



Accurately substituting Fe for Ni₂ atom in Ni-MOF with defect-rich for efficient oxygen evolution reaction: Electronic reconfiguration and mechanistic study

Shifan Zhang^a, Zhiyang Huang^a, Tayirjan Taylor Isimjan^c, Dandan Cai^{a,b,*}, Xiulin Yang^{a,**}

^a Guangxi Key Laboratory of Low Carbon Energy Materials, School of Chemistry and Pharmaceutical Sciences, Guangxi Normal University, Guilin 541004, China

^b School of Chemical Engineering and Technology, Sun Yat-sen University, Zhuhai 519082, China

^c Saudi Arabia Basic Industries Corporation (SABIC) at King Abdullah University of Science and Technology (KAUST), Thuwal 23955-6900, Saudi Arabia

ARTICLE INFO

Keywords:

Bimetallic organic frameworks
Lattice strain
Oxygen vacancy
Oxygen evolution reaction
Electrocatalytic overall water splitting

ABSTRACT

Designing metal-organic framework (MOF) with controllable lattice defects and oxygen vacancies is of great significance for effective oxygen evolution reaction (OER). We achieved controlled lattice defects and generated oxygen vacancies in the Ni-MOF nanoflowers by accurately substituting Fe atoms for Ni₂ atoms. The optimized Ni_{0.67}Fe_{0.33}-MOF/CFP exhibits remarkable OER performance (an ultra-low overpotential of 281 mV at 100 mA cm⁻² and a Tafel slope of 38 mV dec⁻¹) and excellent stability (the activity maintains for 80 h at 100 mA cm⁻²). Importantly, it is revealed that the active species is the Ni_{0.67}Fe_{0.33}-MOF/NiFeOOH complex for OER. Density functional theory (DFT) provides the insightful catalytic mechanism that the Fe atoms and oxygen vacancies are critical in optimizing the *d*-band center and promoting the dissociation of oxygen-containing intermediates. Our work introduces a strategy for designing defect-rich MOF-based electrocatalysts, opening up new possibilities for efficient OER systems.

1. Introduction

The oxygen evolution reaction (OER) plays a vital role in various electrochemical energy storage and conversion technologies [1–3]. However, the OER process, which involves the formation of O-O bonds and a four-proton-coupled electron transfer, often exhibit sluggish kinetics [4–6]. OER kinetics are determined by the rate-determining step (RDS), i.e. the adsorption and desorption of intermediates on the active site [7]; the efficiency of this step is related to the *d*-orbital electronic structure of the active site [8]. Therefore, it is effective to improve the electrochemical performance of electrode materials by tuning the electronic structure of the active site of the electrochemical reaction at the atomic scale. Transition metal-organic frameworks (MOFs) have gained considerable attention in recent years due to their well-dispersed metal sites, uniform pores, and tunable electronic structures [9–11]. However, the limited number of exposed electrochemically active sites and the dense structures of MOFs hinder the formation of active sites, resulting in unsatisfactory electrochemical performance [12].

To overcome these limitations, the concept of introducing subtle defects into nanostructures has emerged, such as multi-metal engineering [13,14], lattice defect engineering [15], and oxygen defect engineering [16]. Among these strategies, lattice defect engineering is a crucial approach for optimizing the electronic structure of nano-materials. Introducing surface and bulk defects through defect engineering can alter atomic and lattice distances [17], thereby influencing the geometrical shape and electronic structure of active sites [18,19], ultimately optimizing the electrocatalytic activity of materials [20]. Previous studies, conducted by Yao et al., induced lattice distortion and dislocations through the electrocatalytic process, resulting in the redistribution of electron density in specific regions and promoting charge and ion transfer [17]. However, the lattice defects generated in these studies were randomly formed during the preparation process. Hence, a controllable approach to inducing lattice defects and establishing the relationship between microstructural lattice defects and active surface sites in MOF remains a significant challenge. Oxygen defect engineering, on the other hand, has shown potential in enhancing the electronic

* Corresponding author at: Guangxi Key Laboratory of Low Carbon Energy Materials, School of Chemistry and Pharmaceutical Sciences, Guangxi Normal University, Guilin 541004, China.

** Corresponding author.

E-mail addresses: caidandan86@163.com (D. Cai), xlyang@gxnu.edu.cn (X. Yang).

<https://doi.org/10.1016/j.apcatb.2023.123448>

Received 4 August 2023; Received in revised form 8 October 2023; Accepted 28 October 2023

Available online 31 October 2023

0926-3373/© 2023 Elsevier B.V. All rights reserved.

conductivity of transition metal catalysts [21], modifying surface adsorption of intermediates, and altering the electronic structure to facilitate charge transfer [22]. Various methods, such as heat treatment, reduction treatment, and plasma etching, have been used to induce a large number of defects under non-equilibrium conditions [23]. For instance, Luo et al. introduced abundant oxygen vacancies into CeO₂ through a high-temperature calcination strategy, which optimized intermediate adsorption/dissociation and improved charge transfer [24]. However, the time-consuming and complex preparation process of oxygen-defective materials has hindered their widespread application and promotion. Thus, there is a need to find an effective and convenient approach to induce oxygen vacancies in electrode materials.

Motivated by these concepts, we have developed a mild and effective strategy to prepare defective Ni_{0.67}Fe_{0.33}-MOF nanoflowers. As expected, the catalyst we prepared exhibits excellent OER activity by adjusting the degree of lattice and oxygen vacancies through the precise substitution of Fe atoms for the Ni2 site in Ni-MOF. Density functional theory (DFT) calculations further validate that the introduction of Fe and the presence of oxygen vacancies can effectively regulate the electron structure and spin state density of the highly active Ni site, balance the adsorption/desorption of intermediates, and minimize the energy barrier of OER. As a result, the intrinsic activity of the catalyst is improved.

2. Experimental section

2.1. Surface modification of the CFP

Prior to the synthesis, the CFP (cut as 1 cm × 2 cm in size) was added to a 25 mL Teflon-lined stainless steel autoclave containing HNO₃ (68 wt %) and maintained at 120 °C for 4 h. Subsequently, the CFP was washed several times with a mixture of water and ethanol until a neutral pH was obtained. Finally, the prepared CFP was stored in an ethanol solution for future use.

2.2. Synthesis of Ni_{1-x}Fe_x-MOF/CFP

0.4 mmol Ni(NO₃)₂·6 H₂O, 0.1 mmol Fe(NO₃)₃·9 H₂O and 0.5 mmol Thiophene-2,5-dicarboxylic acid (H₂TDC) were dissolved in a combination of 6 mL N,N-Dimethylformamide (DMF) and water. The above solution and pre-treated CFP were then transferred into a 25 mL Teflon-lined stainless steel autoclave and heated at 120 °C for 12 h. After cooling to room temperature, the resulting product was washed more than five times with a mixture of water and ethanol to remove impurities. After a 12 h drying period, the resulting brownish-yellow sample has been designated as Ni_{0.67}Fe_{0.33}-MOF/CFP, in accordance with the true Ni and Fe ratio. By varying the proportion of Ni(NO₃)₂·6 H₂O to Fe(NO₃)₃·9 H₂O, we successfully synthesized Ni-MOF/CFP, Ni_{0.80}Fe_{0.20}-MOF/CFP, Ni_{0.21}Fe_{0.79}-MOF/CFP and Fe₂O₃/CFP. The loading of the resulting catalyst on the CFP was about 4.25 mg.

2.3. Synthesis of Ni_{1-x}Fe_x-MOF

The synthesis of Ni_{1-x}Fe_x-MOF powder catalysts followed a similar method to that of Ni_{1-x}Fe_x-MOF/CFP, except that the CFP was not added into the Teflon liner.

3. Results and discussion

3.1. Synthesis and characterizations

According to Fig. 1a, the synthesis of Ni_{0.67}Fe_{0.33}-MOF nanoflowers on CFP was achieved through a one-step hydrothermal method, utilizing H₂TDC as a ligand and Fe(NO₃)₃·9 H₂O and Ni(NO₃)₂·6 H₂O as metal sources. To determine the crystal structure and atomic arrangement, X-ray diffraction (XRD) analysis was performed on the synthesized

samples. As shown in Fig. 1b, the characteristic diffraction peaks of the Ni-MOF material matched well with the theoretical XRD simulation results (CCDC: 716347) [25], indicating the high crystallinity of Ni-MOF and facilitating the preparation of highly crystalline Ni_{1-x}Fe_x-MOF/CFP. The XRD characterization confirmed the well-defined atomic structure of Ni-MOF. Additional details of the ligand TDC²⁻ and its coordination modes are presented in Fig. S1, where the TDC²⁻ ligand exhibited an asymmetric tetradentate (κ¹-κ¹)-(κ¹-κ¹)-μ₄ coordination mode. The compound formed a three-dimensional framework by bridging a chain of repeating structural units [Ni1O₆]₂[Ni2O₆] parallel to the *a*-axis with the two-dentate ligand TDC²⁻. The coordination of Ni atoms in this framework involved octahedral coordination in two ways: (1) Ni1 atom coordination included two μ₃-OH, two oxygen atoms in water molecules, and two ligand oxygen atoms; (2) Ni2 atom coordination included two μ₃-OH and four oxygen atoms from different ligands.

To gain a deeper understanding of the crystal structure of Ni-MOF, the corresponding powder was also subjected to XRD analysis. As depicted in Fig. S2a, the diffraction peaks of in-situ grown Ni-MOF/CFP were similar to those of powdered Ni-MOF, with no noticeable impurity peaks, indicating that they possessed the same crystal structure. High strength peaks at 26° can be attributed to the carbon fiber substrate [26]. Upon the introduction of Fe into Ni-MOF, the diffraction peak of Ni-MOF at 9.1° experienced a slight shift towards a higher angle (9.3°). This transformation can be attributed to the fact that the ionic radius of Fe³⁺ (0.064 nm) is much smaller than that of Ni²⁺ (0.072 nm). When Fe replaces Ni in Ni-MOF, the crystal plane spacing shrinks and lattice distortion occurs, which causes the diffraction peak to shift higher [27].

The introduction of Fe atoms in Ni-MOF plays a crucial role in regulating the degree of grain surface defects. As the Fe atom concentration rises, there's a marked decline in the diffraction peak intensities associated with the (01 $\bar{1}$), (0 $\bar{3}$ 1), (002) and (01 $\bar{2}$) crystal facets. Intriguingly, by the time the Ni/Fe ratio reaches 4, these peaks are almost non-existent, as evidenced in Fig. 1b. Notably, analysis of the MOF structure reveals that these lattice faces are composed of a point lattice of Ni2 atoms in the MOF structure, indicating that Fe atom doping can accurately replace Ni2 atoms, leading to the destruction of the corresponding lattice faces (Fig. S2b). The substitution mechanism is shown in Fig. S3. Consequently, the degree of lattice defects increases with the increasing proportion of Fe atoms replacing Ni2 atoms. When the Ni/Fe ratio is 1, the characteristic diffraction peaks of Ni-MOF completely disappear and exhibit low crystallinity. This suggests that a significant number of Fe atoms further replace Ni1 atoms after the directional substitution of Ni2 atoms, resulting in the disruption of the original ordered structure of Ni-MOF and the generation of numerous lattice defects. Interestingly, XRD analysis reveals that when only single-metal Fe is present, the crystal surface diffraction peaks correspond well with Fe₂O₃ (PDF# 89-0599) (Fig. S4). This indicates that Fe atoms cannot actively coordinate with the ligand to form MOF but can accurately replace Ni2 atoms in Ni-MOF, supporting the previous inference. The Ni/Fe metal atom ratio in Ni_{1-x}Fe_x-MOF was further analyzed by ICP-MS (Table S1), and the results showed that the Ni/Fe metal atom ratio in Ni_{0.67}Fe_{0.33}-MOF/CFP is approximately 2, which is consistent with the conjecture that Fe atom completely replaces Ni2 atomic position.

Raman spectroscopy was further utilized to attest to the successful synthesis of bimetallic Ni_{1-x}Fe_x-MOF/CFP (Fig. S2c). The characteristic peaks observed in the Raman spectrum of Ni_{0.67}Fe_{0.33}-MOF/CFP correspond to those of previously reported NiFe-MOF [28]. Specifically, the peak located at 1470 cm⁻¹ can be attributed to the stretching vibration of ν(COO⁻) [29], while the stretching vibration of ν(C-O), resulting from the deprotonation of hydroxyl groups after coordination, is observed at 1134 cm⁻¹. Additionally, the peaks at 811 cm⁻¹, 688 cm⁻¹, and 562 cm⁻¹ correspond to the bending vibrations of the C-H bond in the thiophene five-membered ring, the bending vibration of the C-S bond, and the vibration of the M-O bond, respectively [30,31]. Importantly,

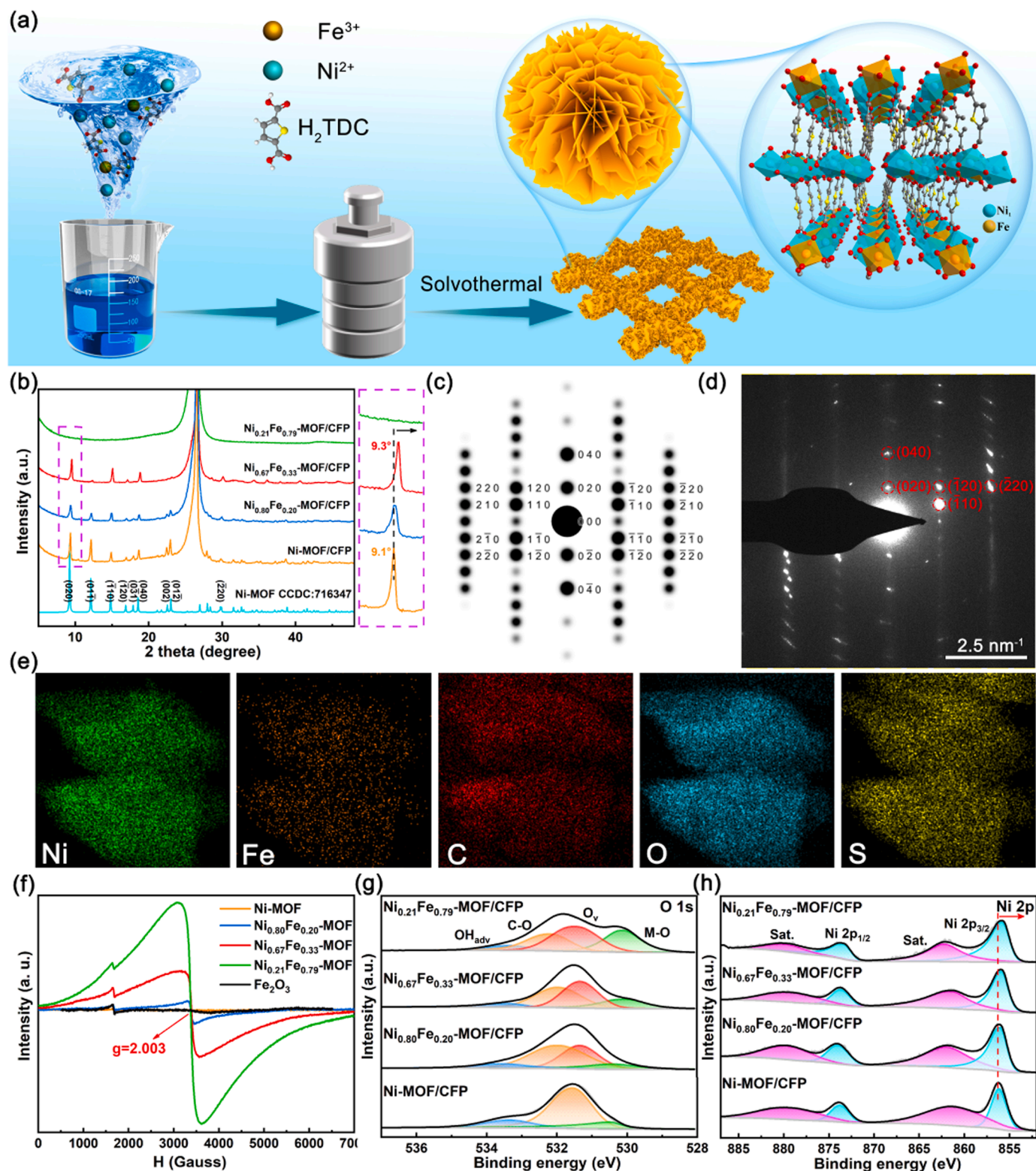


Fig. 1. Design strategy, morphology, and structural characterizations of Ni_{0.67}Fe_{0.33}-MOF/CFP nanoflowers. (a) Schematic illustration of the synthesis of Ni_{0.67}Fe_{0.33}-MOF/CFP nanoflowers, (b) XRD patterns of Ni_{0.21}Fe_{0.79}-MOF/CFP, Ni_{0.67}Fe_{0.33}-MOF/CFP, Ni_{0.80}Fe_{0.20}-MOF/CFP, Ni-MOF/CFP and simulated data from the reported crystal structure, (c) projection along [001] axial SAED model, (d) experimental SAED pattern of Ni_{0.67}Fe_{0.33}-MOF/CFP, and (e) corresponding elemental mapping images of Ni_{0.67}Fe_{0.33}-MOF/CFP. (f) EPR spectra of Ni-MOF, Ni_{0.80}Fe_{0.20}-MOF, Ni_{0.67}Fe_{0.33}-MOF, Ni_{0.21}Fe_{0.79}-MOF and Fe₂O₃. High-resolution O 1s (g) and Ni 2p (h) XPS spectra of Ni-MOF/CFP, Ni_{0.80}Fe_{0.20}-MOF/CFP, Ni_{0.67}Fe_{0.33}-MOF/CFP and Ni_{0.21}Fe_{0.79}-MOF/CFP.

the hypo crystallization caused by the massive doping of Fe to induce lattice defects does not affect the change in the MOF phase.

Morphological and structural analysis of Ni_{0.67}Fe_{0.33}-MOF/CFP was performed using scanning electron microscopy (SEM) and transmission electron microscopy (TEM). The SEM image (Fig. S5a) reveals that Ni_{0.67}Fe_{0.33}-MOF/CFP has a 3D nanoflower morphology, consisting of 1D nanosheets with an average thickness of about 160 nm (Fig. S5b and Fig. S6). This unique structure provides a larger available surface area and superior mass transfer rates compared to disordered and stacked structures. The selected area electron diffraction (SAED) map (Fig. 1d) of Ni_{0.67}Fe_{0.33}-MOF/CFP matches well with the simulated results along the crystal structure's band axis (001) (Fig. 1c), confirming its excellent crystallographic properties. Strong Bragg reflection points of (020), (040), ($\bar{1}10$), ($\bar{1}20$) and ($\bar{2}20$) can be clearly observed, indicating the ultra-high crystallinity of Ni_{0.67}Fe_{0.33}-MOF. Energy dispersive X-ray spectroscopy (EDX) elemental mapping images reveal that Ni, Fe, C, O, and S are uniformly distributed on the surface of Ni_{0.67}Fe_{0.33}-MOF/CFP (Fig. 1e). Additionally, the morphology and microstructure of Ni-MOF/CFP were investigated for comparison. SEM and TEM characterization revealed a rod-shaped morphology for Ni-MOF/CFP with a diameter of approximately 1 μm (Fig. S7a-b). SAED images (Fig. S7c) confirmed the high crystallinity of Ni-MOF/CFP, consistent with the results of Ni_{0.67}Fe_{0.33}-MOF/CFP, thereby indicating the identical crystal structure of both materials, which aligns with the XRD analysis. The high-resolution transmission electron microscopy (HRTEM) image presented in Fig. S8a reveals lattice fringes corresponding to the (020) crystal planes of Ni-MOF-MOF/CFP, exhibiting a spacing of 0.95 nm. Notably, the HRTEM image of Ni_{0.67}Fe_{0.33}-MOF/CFP (Fig. S8b) displays regions with undulating lattice streaks. These distorted streaks can likely be traced back to the lattice defects stemming from Fe atom doping into Ni-MOF, an observation that aligns with prior literature findings [32]. Such induced lattice defects could potentially unveil more active sites, subsequently enhancing the OER reaction's efficiency [15]. Furthermore, EDX analysis shows a uniform distribution of Ni, C, O, and S elements in Ni-MOF/CFP (Fig. S7d). The morphology of the comparison samples Ni_{0.80}Fe_{0.20}-MOF/CFP, Ni_{0.21}Fe_{0.79}-MOF/CFP and Ni_{0.67}Fe_{0.33}-MOF powder is shown in Fig. S9. It can be seen that the morphology of Ni_{0.67}Fe_{0.33}-MOF powder is similar to that of Ni_{0.67}Fe_{0.33}-MOF/CFP. Furthermore, the morphology of Ni_{0.80}Fe_{0.20}-MOF/CFP can be perceived as intermediate between Ni-MOF/CFP and Ni_{0.67}Fe_{0.33}-MOF/CFP. It should be noted that the MOF in Ni_{0.21}Fe_{0.79}-MOF/CFP is in a low crystalline state due to the increase in the proportion of Fe atoms, leading to the disruption of the morphology.

Electron paramagnetic resonance (EPR) characterization was employed to investigate the activated O on the Ni_{1-x}Fe_x-MOF surface. As viewed in Fig. 1f, no EPR signal is observed in Ni-MOF and Fe₂O₃, while bimetallic MOF exhibits an obvious EPR signal with $g = 2.003$, indicating that the introduction of Fe induces the formation of O defects, consistent with the results of O 1 s analysis in XPS [33]. Interestingly, the enhancement of the EPR signal aligns with the increasing Fe doping ratio, namely Ni_{0.21}Fe_{0.79}-MOF > Ni_{0.67}Fe_{0.33}-MOF > Ni_{0.80}Fe_{0.20}-MOF > Ni-MOF.

X-ray photoelectron spectroscopy (XPS) was utilized to investigate the chemical composition and elemental valence states of Ni_{0.67}Fe_{0.33}-MOF/CFP before and after OER testing. It is worth mentioning that the binding energies were calibrated using the C 1 s peak at 284.8 eV [34]. The XPS survey spectrum of Ni_{0.67}Fe_{0.33}-MOF/CFP confirms the presence of Ni, Fe, C, O, and S (Fig. S10), indicating the successful incorporation of Fe. As seen in Fig. 1g, the high-resolution O 1 s spectrum of Ni-MOF/CFP shows characteristic peaks at 530.5 eV, 531.6 eV and 533.3 eV, which are attributed to metal-oxygen (M-O) bond, C-O bond and adsorbed water (H₂O_{ads}), respectively [17]. In the high-resolution O 1 s spectrum of Ni_{0.80}Fe_{0.20}-MOF/CFP, Ni_{0.67}Fe_{0.33}-MOF/CFP and Ni_{0.21}Fe_{0.79}-MOF/CFP, peaks at specific energies 530.0 eV, 531.3 eV, 532.0 eV, and 533.0 eV correspond to the M-O bond, oxygen vacancies

(O_v), C-O bond, and adsorbed H₂O (H₂O_{ads}), respectively [35,36]. The introduction of lattice defects via Fe doping leads to the creation of these oxygen vacancies in Ni-MOF. Such a modification has a consequential impact on the coordination environment and the electronic framework of the O atoms. Specifically, it causes a drop in the binding energy of the M-O bond and an elevation in the binding energy of the C-O bond [37–39]. The change in the M-O bond binding energy suggests that the lattice defects activated lattice oxygen and generated oxygen vacancies, which are beneficial for the catalytic reaction [20]. Notably, the O_v peak intensities in the O 1 s spectra exhibit a gradual increase with the rise in Fe atomic substitution, accompanied by a concurrent increase in M-O bond peak intensities. This phenomenon likely stems from the fact that Fe substitution disrupts the ligand oxygen in the Ni-MOF, leading to the formation of additional Fe-O bonds. Moreover, the results were confirmed by the fact that only Fe₂O₃ was generated by using iron salts during the process of the catalyst preparation.

The Ni 2p high-resolution XPS spectrum of Ni_{0.80}Fe_{0.20}-MOF/CFP, Ni_{0.67}Fe_{0.33}-MOF/CFP and Ni_{0.21}Fe_{0.79}-MOF/CFP (Fig. 1h) was deconvoluted into Ni 2p_{3/2} (855.9 eV), Ni 2p_{1/2} (873.7 eV) and two satellite peaks, indicating the presence of Ni²⁺ [19,40,41]. Notably, compared with Ni-MOF/CFP, the Ni 2p peak of Ni_{1-x}Fe_x-MOF/CFP will be shifted to the lower energy level step by step as the proportion of Fe atoms increases, suggesting that the lattice defects induced by Fe substitution can modulate the electronic structure of the active Ni center [42]. Besides, the Fe 2p spectrum of Ni_{0.80}Fe_{0.20}-MOF/CFP, Ni_{0.67}Fe_{0.33}-MOF/CFP and Ni_{0.21}Fe_{0.79}-MOF/CFP manifests that the peaks located at 711.0 eV and 724.2 eV are assigned to 2p_{3/2} and 2p_{1/2} of Fe³⁺, respectively (Fig. S11) [30]. In summary, the introduction of lattice defects by Fe atom doping in Ni-MOF/CFP results in the formation of oxygen vacancies. This in turn impacts the electronic structures of both Ni and Fe atoms, leading to shifts in the binding energies of Ni 2p and Fe 2p [38]. This shift in energy promotes more efficient electron transfer between metal centers, particularly from Fe to Ni. This suggests a more pronounced electronic interaction between Ni and Fe, allowing for a greater number of electrons to populate the Ni's e_g orbital. However, due to the stronger overlap between the e_g orbitals involved in σ -bonding and the oxygen-related adsorbate compared to the t_{2g} orbitals involved in π -bonding, they can more directly facilitate the electron transfer between the surface cation and the adsorbate intermediate in catalytic reactions [43]. Such dynamics considerably hasten the adsorption/desorption cycles of oxygen-rich species like OH* , OOH, and O, thereby amplifying the OER activity [44].

3.2. Electrocatalytic OER activities

A series of catalysts were evaluated for their OER performance in 1.0 M KOH using a typical three-electrode system. Based on the linear sweep voltammetry (LSV) curves that were calibrated to the reversible hydrogen electrode (RHE) and resistance (*i*R) corrected (Fig. 2a), Ni_{0.67}Fe_{0.33}-MOF/CFP exhibits the lowest overpotential of 281 mV at 100 mA cm⁻², significantly superior to that of Ni-MOF/CFP, Ni_{0.80}Fe_{0.20}-MOF/CFP, Ni_{0.21}Fe_{0.79}-MOF/CFP, Fe₂O₃/CFP and RuO₂/CFP. Owing to the presence of an oxidation peak in Ni_{0.67}Fe_{0.33}-MOF/CFP, the reverse LSV test was performed, yielding an overpotential of only 230 mV at 10 mA cm⁻² (Fig. S12). Notably, both Ni_{0.67}Fe_{0.33}-MOF/CFP and Ni-MOF/CFP exhibit an anodic oxidation peak, which can be attributed to the oxidation of Ni²⁺ to Ni^{3/4+} and deprotonation of hydroxyl groups, confirming the surface reconstruction of MOF into hydroxides [45,46]. Additionally, the Tafel slope is an important indicator to evaluate the OER reaction kinetics. The Tafel slopes were calculated from the reverse LSV data of Ni_{1-x}Fe_x-MOF/CFP catalysts. As described in Fig. 2b, The Tafel slope value (38 mV dec⁻¹) of Ni_{0.67}Fe_{0.33}-MOF/CFP is smaller than that of Ni-MOF/CFP (68 mV dec⁻¹), Ni_{0.80}Fe_{0.20}-MOF/CFP (43 mV dec⁻¹), Ni_{0.21}Fe_{0.79}-MOF/CFP (47 mV dec⁻¹), Fe₂O₃/CFP (44 mV dec⁻¹) and RuO₂/CFP (85 mV dec⁻¹), confirming that Ni_{0.67}Fe_{0.33}-MOF/CFP exhibits the most effective catalytic kinetics.

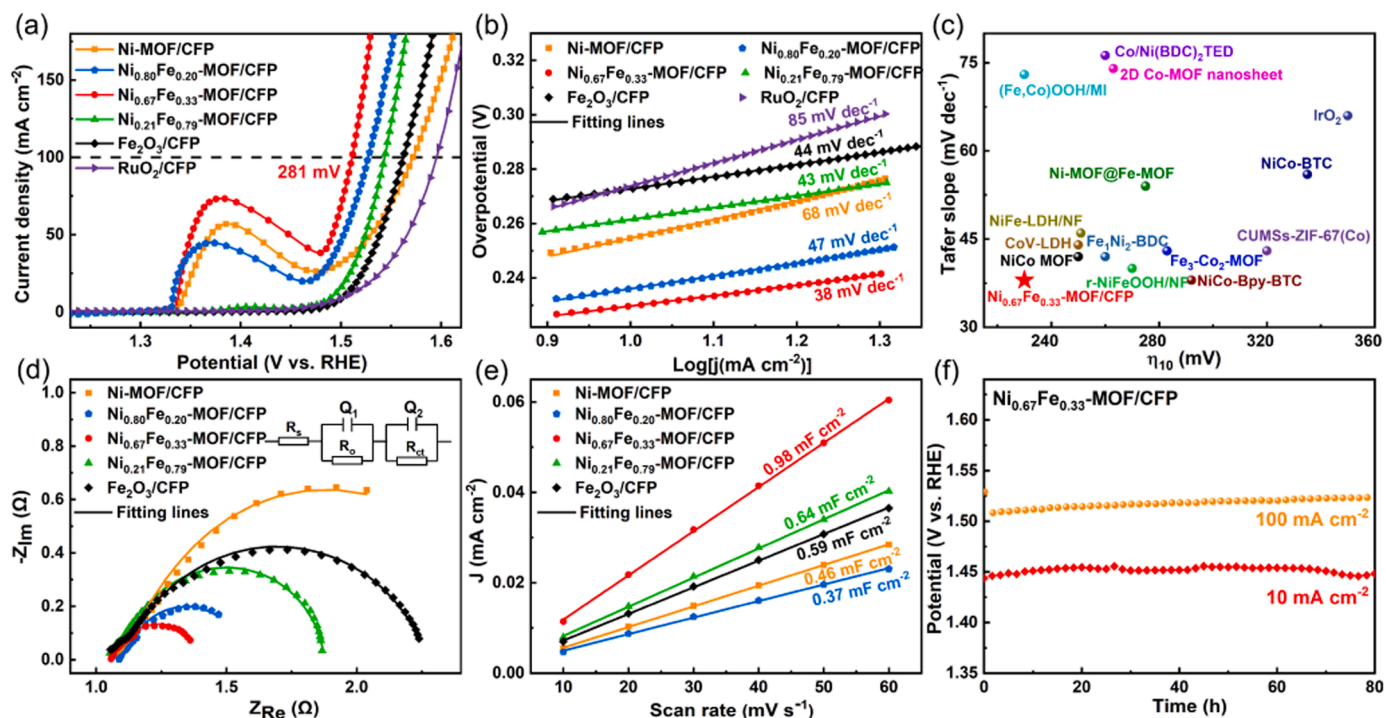


Fig. 2. Electrochemical OER tests in 1.0 M KOH electrolyte using a three-electrode system for Ni-MOF/CFP, Ni_{0.80}Fe_{0.20}-MOF/CFP, Ni_{0.67}Fe_{0.33}-MOF/CFP, Ni_{0.21}Fe_{0.79}-MOF/CFP, Fe₂O₃/CFP and RuO₂/CFP. (a) LSV polarization curves, (b) Tafel slopes, (c) comparison of the overpotential at 100 mA cm⁻² and Tafel slope with previously reported catalysts, (d) double-layer capacitance (C_{dl}) plots, (e) Nyquist plots and (f) chronopotentiometry of Ni_{0.67}Fe_{0.33}-MOF/CFP at 10 and 100 mA cm⁻².

However, the OER electrocatalytic trend is slightly different from the EPR trend. This can be attributed to the beneficial effect of appropriate O vacancies, which help tune the electronic structure and intermediates of metal compounds [20,47], and provide additional active sites for the material, thereby reducing the overpotential required for the reaction [48,49]. Among them, Ni_{0.67}Fe_{0.33}-MOF/CFP showcases a higher concentration of oxygen vacancies relative to both Ni-MOF/CFP and Ni_{0.80}Fe_{0.20}-MOF/CFP. Compared to the low-crystalline structure of Ni_{0.21}Fe_{0.79}-MOF/CFP, Ni_{0.67}Fe_{0.33}-MOF/CFP retains the structure of MOF due to the appropriate lattice defects. Therefore, Ni_{0.67}Fe_{0.33}-MOF/CFP exhibits the highest electrochemical activity due to the combined effect of oxygen vacancies and lattice defects.

It is noteworthy that the overpotential (η_{10}) and Tafel slope of Ni_{0.67}Fe_{0.33}-MOF/CFP are significantly lower than those of other excellent OER catalysts reported recently (Fig. 2c). To further understand the catalytic kinetics of OER process, electrochemical impedance spectroscopy (EIS) was performed. As viewed in Fig. 2d, Ni_{0.67}Fe_{0.33}-MOF/CFP displays a smaller semicircle diameter than Ni-MOF/CFP, Ni_{0.80}Fe_{0.20}-MOF/CFP, Ni_{0.21}Fe_{0.79}-MOF/CFP and Fe₂O₃/CFP, demonstrating faster charge transfer and better electrical conductivity of Ni_{0.67}Fe_{0.33}-MOF/CFP. The electrochemical active surface area (ECSA) of the samples was assessed by measuring the double-layer capacitance (C_{dl}) to understand the source of the remarkable OER activity (Fig. S13 and Fig. 2e). Ni_{0.67}Fe_{0.33}-MOF/CFP exhibited the highest C_{dl} (0.98 mF cm⁻²), indicating a maximal specific surface area and the exposure of more active sites. Meanwhile, the intrinsic catalytic prowess of the catalysts was assessed through the computation of the turnover frequency (TOF), leveraging the results from ICP-MS (Table S1). Notably, the TOF value for Ni_{0.67}Fe_{0.33}-MOF/CFP overshadowed those of other catalysts at an equivalent potential, underscoring its exceptional OER conversion efficiency and potent intrinsic catalytic activity [50]. From the standpoint of mass-specific activity, Ni_{0.67}Fe_{0.33}-MOF/CFP stood out remarkably. At an overpotential of 300 mV, it boasted mass current densities that were triple and quadruple those of Ni-MOF/CFP and

Fe₂O₃/CFP, respectively (refer to Fig. S14b). Additionally, long-term stability is an essential criterion for evaluating the practical application value of electrocatalysts. Remarkably, Ni_{0.67}Fe_{0.33}-MOF/CFP demonstrated extraordinary OER stability with no significant potential change at 10 and 100 mA cm⁻² over 80 h (Fig. 2f).

3.3. Analyzing the dynamic transformation of catalysts during the OER process

After OER test, the Ni 2p high-resolution XPS spectrum of Ni_{0.67}Fe_{0.33}-MOF/CFP is indexed to Ni 2p_{3/2} (855.6 eV) and Ni 2p_{1/2} (873.5 eV) of Ni²⁺, Ni 2p_{3/2} (856.8 eV) and Ni 2p_{1/2} (875.3 eV) of Ni³⁺, and corresponding satellite peaks (Fig. 3a). Importantly, the Ni 2p peak shifts towards higher binding energy by 0.17 eV after OER testing, indicating that high-valence Ni³⁺/Ni⁴⁺ is formed on the surface of Ni_{0.67}Fe_{0.33}-MOF/CFP after OER, which facilitates efficient and rapid electron transfer during OER [51]. In addition, the Fe 2p spectra were shifted towards higher binding energies after the OER test, although no new peaks appeared (Fig. 3b). In the O 1s spectrum, the intensity of the lattice oxygen peak exhibits a decreasing trend after the OER, suggesting that the lattice oxygen obtained through the lattice defect strategy contributes to the catalytic reaction [20]. In summary, these shifts indicate electron transfer between Fe and Ni through the bridging oxygen of the ligand, while oxygen atoms serve as intermediates between various metal atoms to maintain charge balance and strengthen metal-metal interactions.

In addition to the abundant defects, Fe species also play a crucial role in promoting the OER activity of Ni_{0.67}Fe_{0.33}-MOF/CFP. To understand the true catalytic sites and the key role of Fe sites in the catalytic system, a series of characterizations were performed on Ni_{0.67}Fe_{0.33}-MOF/CFP after electrochemical test, including XRD, EPR, XPS, SEM, TEM and electrochemical in situ Raman spectroscopy. As shown in Fig. S15a-b, Ni_{0.67}Fe_{0.33}-MOF/CFP retains nanosheet morphology. The SAED pattern (Fig. S15c) shows diffuse diffraction rings, indicating that the MOF has

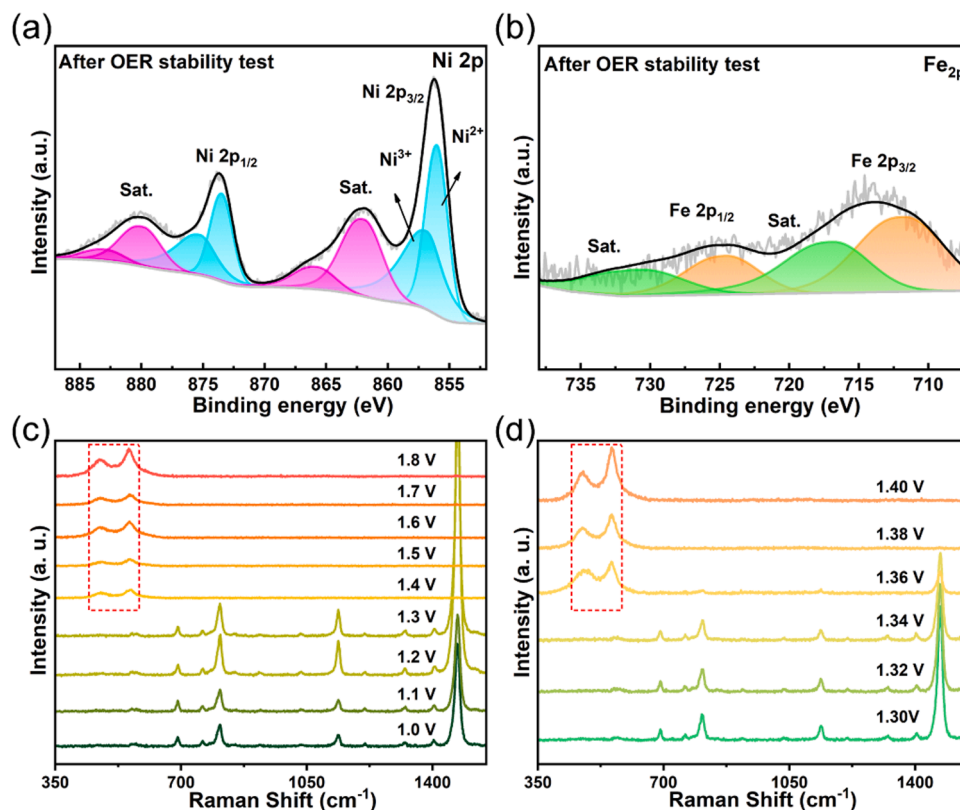


Fig. 3. High-resolution XPS spectra of $\text{Ni}_{0.67}\text{Fe}_{0.33}\text{-MOF/CFP}$ after OER stability test, (a) Ni 2p, and (b) Fe 2p. Electrochemical in situ Raman spectra of (c) $\text{Ni}_{0.67}\text{Fe}_{0.33}\text{-MOF/CFP}$ in the potential range of 1.00–1.80 V (vs. RHE) and (d) $\text{Ni}_{0.67}\text{Fe}_{0.33}\text{-MOF/CFP}$ in the potential range of 1.30–1.40 V (vs. RHE).

been transformed into a lower crystalline state [52]. Notably, some diffraction rings correspond to those of NiFeOOH (PDF# 14-0117), demonstrating that the MOF has been partially transformed into NiFeOOH , and $\text{Ni}_{0.67}\text{Fe}_{0.33}\text{-MOF/NiFeOOH}$ is the true active species of the OER reaction. The post-electrochemical reaction XRD spectra, as illustrated in Fig. S16, reveal that the characteristic MOF peaks are partially preserved. The emergence of additional peaks can be attributed to NiFeOOH , further corroborating the aforementioned characterization. As demonstrated in the EPR and high-resolution O 1s spectra (Fig. S17), it is noteworthy that the characteristic peak associated with oxygen vacancies persists even after the electrochemical reaction of $\text{Ni}_{0.67}\text{Fe}_{0.33}\text{-MOF/CFP}$. EDS mapping images manifest a homogeneous distribution of Ni, Fe, C, O and S (Fig. S15d). And the presence of S confirms the retention of MOF.

To further understand the surface reconstruction process, electrochemical in situ Raman spectroscopy was employed to analyze the structural transformation of $\text{Ni}_{0.67}\text{Fe}_{0.33}\text{-MOF/CFP}$ and Ni-MOF/CFP in the potential range of 1.00–1.80 V. As shown in Fig. 3c, no significant changes were observed in Raman features of $\text{Ni}_{0.67}\text{Fe}_{0.33}\text{-MOF/CFP}$ at 1.00–1.30 V (vs. RHE), indicating that the Ni species have not undergone oxidation at this stage. However, when the potential reaches 1.40 V (vs. RHE), the Raman characteristic peaks of MOF disappeared, and two distinct signal peaks are detected at $\sim 474\text{ cm}^{-1}$ and 554 cm^{-1} , corresponding to the E_g bending and A_1g stretching vibrations of Ni/Fe-O in NiFeOOH [51,53,54]. The Raman spectra of Ni-MOF/CFP exhibit a similar phase transition to NiFeOOH in the potential range of 1.30–1.40 V (Fig. S18a).

Further in situ Raman spectra were then investigated in the potential range of 1.30–1.40 V (vs. RHE) at 0.02 V intervals (Fig. 3d and Fig. S18b). At 1.34 V (vs. RHE), the characteristic peaks of $\text{Ni}_{0.67}\text{Fe}_{0.33}\text{-MOF/CFP}$ remain unchanged, while those of Ni-MOF disappear, indicating that $\text{Ni}_{0.67}\text{Fe}_{0.33}\text{-MOF/CFP}$ exhibits better electrocatalytic stability compared to Ni-MOF/CFP . Subsequently, when the potential

reaches 1.36 V (vs. RHE), both $\text{Ni}_{0.67}\text{Fe}_{0.33}\text{-MOF/CFP}$ and Ni-MOF/CFP exhibit characteristic peaks of NiOOH . However, the intensity of the NiFeOOH characteristic peak in Ni-MOF/CFP is weaker than that in $\text{Ni}_{0.67}\text{Fe}_{0.33}\text{-MOF/CFP}$, indicating that the oxidation potential required for the formation of NiFeOOH active species is lower for $\text{Ni}_{0.67}\text{Fe}_{0.33}\text{-MOF/CFP}$. This difference can be attributed to the presence of Fe species and oxygen vacancies, which lower the oxidation potential required for the formation of the high-valence active hydroxide species of NiFe [42, 53,55]. The coordinated electronic structure of oxygen vacancies further promotes the formation of highly active metal hydroxides by accelerating charge transfer [48,56].

3.4. OER mechanism investigation by DFT theoretical simulation

To elucidate the intrinsic OER catalytic mechanism of the $\text{Ni}_{0.67}\text{Fe}_{0.33}\text{-MOF/NiFeOOH}$ composite interface, theoretical investigations based on DFT calculations were conducted. Charge density analysis reveals visible charge accumulation at the interface, effectively confirming strong electronic interaction between $\text{Ni}_{0.67}\text{Fe}_{0.33}\text{-MOF}$ (Ni-MOF) and NiFeOOH (NiOOH) (Fig. 4a-c and Fig. S19) [57]. Notably, compared to Ni-MOF/NiOOH , the charge on Ni/Fe atoms in $\text{Ni}_{0.67}\text{Fe}_{0.33}\text{-MOF/NiFeOOH}$ was found to significantly accumulate on the O atoms, indicating that electrons transfer from Ni/Fe to adjacent O atoms, which is consistent with the XPS results after electrochemistry. This can be attributed to the fact that the defective O atoms in $\text{Ni}_{0.67}\text{Fe}_{0.33}\text{-MOF/NiFeOOH}$ can accommodate more charges [20]. The transfer of electrons from Ni/Fe to the neighboring O atoms will lead to an increase in the highly valent active sites of Ni/Fe, which effectively promotes the rapid OER-catalyzed reaction [58,59]. Based on the four-step mechanism of adsorbate evolution under alkaline conditions, the optimal models and corresponding geometries of various intermediates of $\text{Ni}_{0.67}\text{Fe}_{0.33}\text{-MOF/NiFeOOH}$ were shown in Fig. 4d. For comparison, the OER process of Ni-MOF/NiOOH was calculated

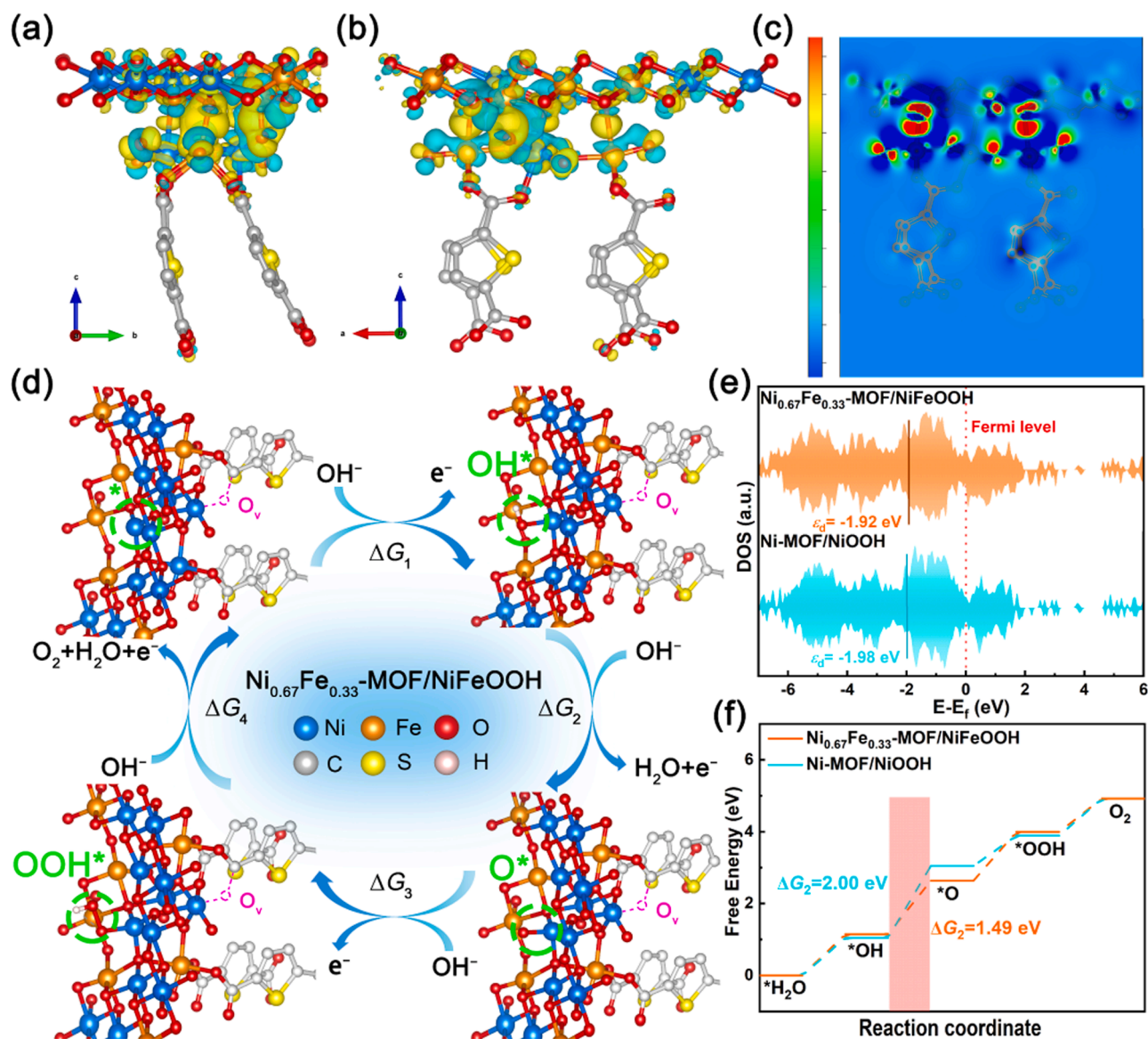


Fig. 4. Differential charge density diagrams of $\text{Ni}_{0.67}\text{Fe}_{0.33}\text{-MOF/NiFeOOH}$ (a) side view, (b) main view, and (c) 2D dimensional charge density map. Yellow and cyan regions represent charge accumulation and depletion, respectively. (d) OER mechanism illustration of $\text{Ni}_{0.67}\text{Fe}_{0.33}\text{-MOF/NiFeOOH}$. (e) The density of state (DOS), and (f) Gibbs free energy diagrams of $\text{Ni}_{0.67}\text{Fe}_{0.33}\text{-MOF/NiFeOOH}$ and Ni-MOF/NiOOH .

(Fig. S20). Furthermore, the density of states (DOS) and d -band center (ϵ_d) of $\text{Ni}_{0.67}\text{Fe}_{0.33}\text{-MOF/NiFeOOH}$ and Ni-MOF/NiOOH were calculated to gain a deeper understanding of the electronic structure changes in the catalyst. As seen in Fig. 4e, $\text{Ni}_{0.67}\text{Fe}_{0.33}\text{-MOF/NiFeOOH}$ has enhanced DOS near the Fermi level compared to Ni-MOF/NiOOH , indicating that $\text{Ni}_{0.67}\text{Fe}_{0.33}\text{-MOF/NiFeOOH}$ possesses better conductivity [60,61]. Moreover, the ϵ_d of $\text{Ni}_{0.67}\text{Fe}_{0.33}\text{-MOF/NiFeOOH}$ is -1.92 eV, closer to the Fermi level than Ni-MOF/NiOOH ($\epsilon_d = -1.98$ eV), indicating that the introduction of Fe can effectively optimize the electronic structure and d -band center of Ni sites [42], thereby enhancing the adsorption capacity of the materials to the intermediates [62]. Finally, the activity of metals towards OER was analyzed by calculating the Gibbs free energy. Generally, the step with the largest change in Gibbs free energy (ΔG) in the four-electron transfer steps of alkaline OER is determined as the rate-determining step (RDS) [63]. As shown in Fig. 4f, although the RDS of $\text{Ni}_{0.67}\text{Fe}_{0.33}\text{-MOF/NiFeOOH}$ and Ni-MOF/NiOOH are both the second step ($\text{*OH} \rightarrow \text{*O}$), the ΔG_2 of $\text{Ni}_{0.67}\text{Fe}_{0.33}\text{-MOF/NiFeOOH}$ is 1.49 eV much lower than that of Ni-MOF/NiOOH (2.00 eV), which reveals a lower theoretical onset overpotential (0.26 V) and more

favorable OER kinetics of $\text{Ni}_{0.67}\text{Fe}_{0.33}\text{-MOF/NiFeOOH}$ [35], and the enhanced OER activity of bimetallic $\text{Ni}_{0.67}\text{Fe}_{0.33}\text{-MOF/NiFeOOH}$ with oxygen vacancies. Therefore, the computational results are consistent with experimental observations.

Charge transfer processes and electronic interactions were also elucidated from the point of view of the electronic structure of the d -orbital in $\text{Ni}_{0.67}\text{Fe}_{0.33}\text{-MOF/NiFeOOH}$. In Ni^{2+} ($t_{2g}^6 e_g^2$) and Ni^{3+} ($t_{2g}^5 e_g^1$) ions, the π -symmetric (t_{2g}) d -orbital are fully occupied, resulting in strong electron-electron repulsive interactions with the bridging oxygen [64]. In contrast, the valence electron configuration of the Fe^{3+} ion is ($t_{2g}^3 e_g^2$), which corresponds to a π -symmetric (t_{2g}) d -orbital with three unpaired electrons. Therefore, the electronic interaction between the bridging oxygen and Fe^{3+} is relatively weak [65]. Compared with Ni-MOF/NiOOH , the Ni-O-Fe bond formed by $\text{Ni}_{0.67}\text{Fe}_{0.33}\text{-MOF/NiFeOOH}$ will lead to electron-electron repulsion between Ni and oxygen enhancing the π -donation energy of Fe-O due to the coupling between Ni^{2+} (Ni^{3+}) and Fe^{3+} , prompting the electron transfer from Ni to Fe [66]. With the decrease of electron density at the Ni site, Ni^{2+} (Ni^{3+}) with low half-full e_g orbital will form proper binding with adsorbed oxygen,

which will be favorable to improve the catalytic activity of OER and accelerate the reaction rate [67]. In summary, the presence of Fe in $\text{Ni}_{0.67}\text{Fe}_{0.33}\text{-MOF/NiFeOOH}$ makes Ni^{2+} more difficult to oxidize, resulting in $\text{Ni}^{3+/4+}$ having a stronger oxidizing ability and therefore faster OER kinetics [68,69].

3.5. Overall water splitting analysis

Inspired by the outstanding OER performance of $\text{Ni}_{0.67}\text{Fe}_{0.33}\text{-MOF/CFP}$, a two-electrode system was assembled with $\text{Ni}_{0.67}\text{Fe}_{0.33}\text{-MOF/CFP}$ and Pt/C as the respective anode and cathode ($\text{Ni}_{0.67}\text{Fe}_{0.33}\text{-MOF/CFP}^{(+)} \parallel \text{Pt/C}^{(-)}$) to assess the potential of overall water splitting (Fig. 5a). As displayed in Fig. 5b, the $\text{Ni}_{0.67}\text{Fe}_{0.33}\text{-MOF/CFP}^{(+)} \parallel \text{Pt/C}^{(-)}$ electrolyzer requires only 1.48 and 1.71 V to reach current densities of 10 and 200 mA cm^{-2} , respectively, significantly lower than that of $\text{RuO}_2^{(+)} \parallel \text{Pt/C}^{(-)}$ (1.53 and 1.92 V for 10 and 200 mA cm^{-2}). Additionally, the overall water-splitting performance of $\text{Ni}_{0.67}\text{Fe}_{0.33}\text{-MOF}$ surpasses most advanced electrocatalysts reported in the literature (Fig. 5c and Table S3). The electrochemical durability of $\text{Ni}_{0.67}\text{Fe}_{0.33}\text{-MOF/CFP}^{(+)} \parallel \text{Pt/C}^{(-)}$ was further studied via chronoamperometry testing. As illustrated in Fig. 5d, $\text{Ni}_{0.67}\text{Fe}_{0.33}\text{-MOF/CFP}^{(+)} \parallel \text{Pt/C}^{(-)}$ can operate normally for 80 h at current density of 200 mA cm^{-2} . These results demonstrate that $\text{Ni}_{0.67}\text{Fe}_{0.33}\text{-MOF/CFP}$ is a promising non-noble metal alternative with notable stability and excellent activity.

4. Conclusions

In summary, we have prepared an efficient and stable $\text{Ni}_{0.67}\text{Fe}_{0.33}\text{-MOF/CFP}$ electrocatalyst using a one-step mild solvothermal method. Structural characterization and elemental analysis manifest that the introduction of Fe atoms precisely replaces the Ni site in Ni-MOF, triggering controllable lattice defects and generating oxygen vacancies. The optimal $\text{Ni}_{0.67}\text{Fe}_{0.33}\text{-MOF/CFP}$ exhibits excellent catalytic activity (281 mV @ 100 mA cm^{-2}) and long-term stability

(80 h @ 100 mA cm^{-2}) in an alkaline medium. Furthermore, the fabricated $\text{Ni}_{0.67}\text{Fe}_{0.33}\text{-MOF/CFP}^{(+)} \parallel \text{Pt/C}^{(-)}$ just need ultra-low cell voltage of 1.48 and 1.71 V to reach current densities of 10 and 200 mA cm^{-2} , respectively, superior to those of $\text{RuO}_2^{(+)} \parallel \text{Pt/C}^{(-)}$. Meanwhile, the $\text{Ni}_{0.67}\text{Fe}_{0.33}\text{-MOF/CFP}$ -based electrolyzer can operate stably for 80 h at the current density of 200 mA cm^{-2} without significant attenuation, indicating its good durability. In situ Raman analysis confirms that $\text{Ni}_{0.67}\text{Fe}_{0.33}\text{-MOF/NiFeOOH}$ is the active species in OER catalysis. Experimental and DFT calculations result prove that the introduction of Fe atoms and the presence of oxygen vacancies in $\text{Ni}_{0.67}\text{Fe}_{0.33}\text{-MOF/NiFeOOH}$ effectively modify the electronic structure of the Ni site to move the *d*-band center towards the Fermi level, optimize the desorption process of $^*\text{OH}$ intermediates, and promote the charge transfer process in OER. This work provides a new perspective for introducing multi-defect coordinated unsaturated metal site regulation of MOF as an efficient electrocatalyst.

CRediT authorship contribution statement

Shifan Zhang: Writing – original draft, Investigation, Formal analysis, Methodology. **Zhiyang Huang:** Data curation, Conceptualization. **Tayirjan Taylor Isimjan:** Writing – review & editing. **Dandan Cai:** Supervision, Writing – review & editing, Validation, Funding acquisition. **Xiulin Yang:** Supervision, Writing – review & editing, Funding acquisition.

Declaration of Competing Interest

The authors declare that they have no known competing financial interests or personal relationships that could have appeared to influence the work reported in this paper.

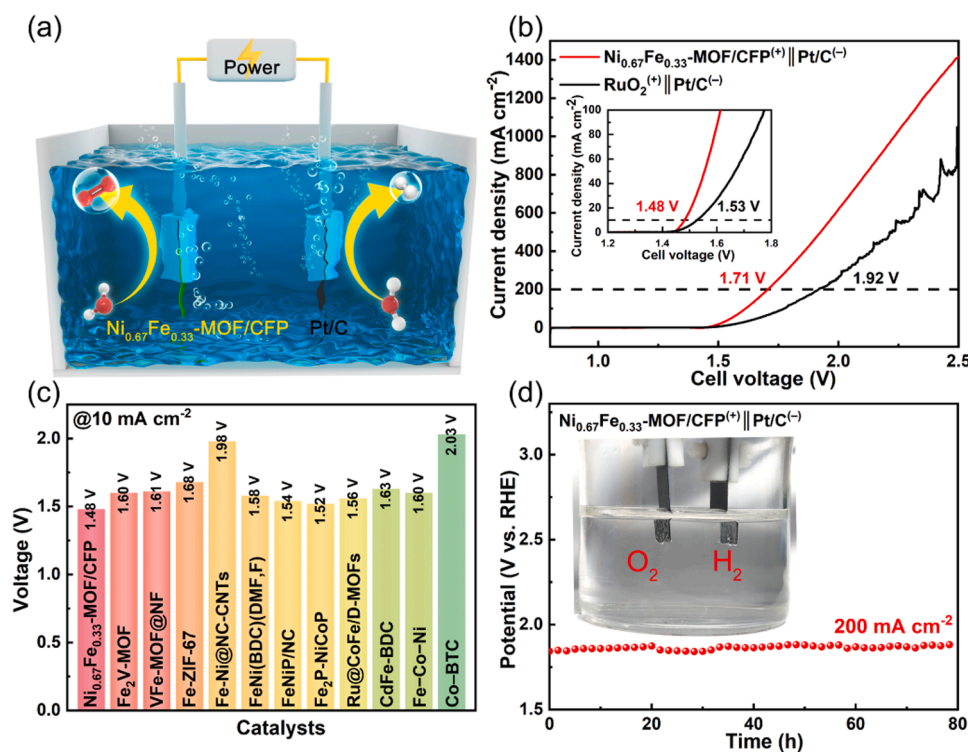


Fig. 5. (a) Schematic diagram of overall water splitting in two-electrode system, (b) polarization curves of $\text{Ni}_{0.67}\text{Fe}_{0.33}\text{-MOF/CFP}^{(+)} \parallel \text{Pt/C}^{(-)}$ and $\text{RuO}_2^{(+)} \parallel \text{Pt/C}^{(-)}$ for overall water splitting in 1.0 M KOH, (c) comparison the cell voltage at 10 mA cm^{-2} with previously reported catalysts in 1.0 M KOH, and (d) chronoamperometry test at 200 mA cm^{-2} .

Data Availability

The data that support the findings of this study are available from the corresponding author upon reasonable request.

Acknowledgements

This work was financially supported by the National Natural Science Foundation of China (No. 22068008, 21965005), Guangxi Province Natural Science Foundation (No. 2020GXNSFAA159104, 2019GXNSFGA245003), and Innovation Project of Guangxi Graduate Education (YCBZ2023062, YCSW2023140).

Appendix A. Supporting information

Supplementary data associated with this article can be found in the online version at [doi:10.1016/j.apcatb.2023.123448](https://doi.org/10.1016/j.apcatb.2023.123448).

References

- Y.Z. Wang, M. Yang, Y.-M. Ding, N.-W. Li, L. Yu, Recent advances in complex hollow electrocatalysts for water splitting, *Adv. Funct. Mater.* 32 (2022), 2108681, <https://doi.org/10.1002/adfm.202108681>.
- Z.-Y. Yu, Y. Duan, X.-Y. Feng, X. Yu, M.-R. Gao, S.-H. Yu, Clean and affordable hydrogen fuel from alkaline water splitting: past, recent progress, and future prospects, *Adv. Mater.* 33 (2021), 2007100, <https://doi.org/10.1002/adma.202007100>.
- X. Ren, T. Wu, Y. Sun, Y. Li, G. Xian, X. Liu, C. Shen, J. Gracia, H.-J. Gao, H. Yang, Z.J. Xu, Spin-polarized oxygen evolution reaction under magnetic field, *Nat. Commun.* 12 (2021), 2608, <https://doi.org/10.1038/s41467-021-22865-y>.
- R.R. Rao, S. Corby, A. Bucci, M. García-Teedor, C.A. Mesa, J. Rossmeisl, S. Giménez, J. Lloret-Fillol, I.E.L. Stephens, J.R. Durrant, Spectroelectrochemical analysis of the water oxidation mechanism on doped nickel oxides, *J. Am. Chem. Soc.* 144 (2022) 7622–7633, <https://doi.org/10.1021/jacs.1c08152>.
- X.L. Wang, L.Z. Dong, M. Qiao, Y.J. Tang, J. Liu, Y. Li, S.L. Li, J.X. Su, Y.Q. Lan, Exploring the performance improvement of the oxygen evolution reaction in a stable bimetal-organic framework system, *Angew. Chem. Int. Ed.* 57 (2018) 9660–9664, <https://doi.org/10.1002/anie.201803587>.
- P. Wang, M. Yan, J. Meng, G. Jiang, L. Qu, X. Pan, J.Z. Liu, L. Mai, Oxygen evolution reaction dynamics monitored by an individual nanosheet-based electronic circuit, *Nat. Commun.* 8 (2017), 645, <https://doi.org/10.1038/s41467-017-00778-z>.
- C. Casadevall, V. Martin-Diaconescu, W.R. Browne, S. Fernández, F. Franco, N. Cabello, J. Benet-Buchholz, B. Lassalle-Kaiser, J. Lloret-Fillol, Isolation of a Ru (iv) side-on peroxo intermediate in the water oxidation reaction, *Nat. Chem.* 13 (2021) 800–804, <https://doi.org/10.1038/s41557-021-00702-5>.
- Y. Sun, S. Sun, H. Yang, S. Xi, J. Gracia, Z.J. Xu, Spin-related electron transfer and orbital interactions in oxygen electrocatalysis, *Adv. Mater.* 32 (2020), 2003297, <https://doi.org/10.1002/adma.202003297>.
- J. Meng, X. Liu, C. Niu, Q. Pang, J. Li, F. Liu, Z. Liu, L. Mai, Advances in metal-organic framework coatings: versatile synthesis and broad applications, *Chem. Soc. Rev.* 49 (2020) 3142–3186, <https://doi.org/10.1039/C9CS00806C>.
- W. Zhou, D.D. Huang, Y.P. Wu, J. Zhao, T. Wu, J. Zhang, D.S. Li, C. Sun, P. Feng, X. Bu, Stable hierarchical bimetal-organic nanostructures as high-performance electrocatalysts for the oxygen evolution reaction, *Angew. Chem. Int. Ed.* 58 (2019) 4227–4231, <https://doi.org/10.1002/anie.201813634>.
- Y. Jia, Z. Xue, Y. Li, G. Li, Recent progress of metal organic frameworks-based electrocatalysts for hydrogen evolution, oxygen evolution, and oxygen reduction reaction, *Energy Environ. Mater.* 5 (2022) 1084–1102, <https://doi.org/10.1002/eem2.12290>.
- P.-Q. Liao, J.-Q. Shen, J.-P. Zhang, Metal-organic frameworks for electrocatalysis, *Coord. Chem. Rev.* 373 (2018) 22–48, <https://doi.org/10.1016/j.ccr.2017.09.001>.
- J.S. Kim, B. Kim, H. Kim, K. Kang, Recent progress on multimetal oxide catalysts for the oxygen evolution reaction, *Adv. Energy Mater.* 8 (2018), 1702774, <https://doi.org/10.1002/aenm.201702774>.
- C.-T. Dinh, A. Jain, F.P.G. de Arquer, P. De Luna, J. Li, N. Wang, X. Zheng, J. Cai, B. Z. Gregory, O. Voznyy, B. Zhang, M. Liu, D. Sinton, E.J. Crumlin, E.H. Sargent, Multi-site electrocatalysts for hydrogen evolution in neutral media by destabilization of water molecules, *Nat. Energy* 4 (2019) 107–114, <https://doi.org/10.1038/s41560-018-0296-8>.
- Y. Sun, K. Xu, Z. Wei, H. Li, T. Zhang, X. Li, W. Cai, J. Ma, H.J. Fan, Y. Li, Strong electronic interaction in dual-cation-incorporated NiSe₂ nanosheets with lattice distortion for highly efficient overall water splitting, *Adv. Mater.* 30 (2018), 1802121, <https://doi.org/10.1002/adma.201802121>.
- Z.-Y. Yu, Y. Duan, J.-D. Liu, Y. Chen, X.-K. Liu, W. Liu, T. Ma, Y. Li, X.-S. Zheng, T. Yao, M.-R. Gao, J.-F. Zhu, B.-J. Ye, S.-H. Yu, Unconventional CN vacancies suppress iron-leaching in Prussian blue analogue pre-catalyst for boosted oxygen evolution catalysis, *Nat. Commun.* 10 (2019), 2799, <https://doi.org/10.1038/s41467-019-10698-9>.
- S. Yao, Y. Jiao, C. Lv, Y. Kong, S. Ramakrishna, G. Chen, Lattice-strain engineering of CoOOH induced by NiMn-MOF for high-efficiency supercapacitor and water oxidation electrocatalysis, *J. Colloid Interface Sci.* 623 (2022) 1111–1121, <https://doi.org/10.1016/j.jcis.2022.04.126>.
- D. Sun, L.W. Wong, H.Y. Wong, K.H. Lai, L. Ye, X. Xu, T.H. Ly, Q. Deng, J. Zhao, Direct Visualization of Atomic Structure in Multivariate Metal-organic Frameworks (MOFs) for guiding electrocatalysts design, *Angew. Chem. Int. Ed.* 62 (2023), e202216008, <https://doi.org/10.1002/anie.202216008>.
- Y. Yang, S. Wei, Y. Li, D. Guo, H. Liu, L. Liu, Effect of cobalt doping-regulated crystallinity in nickel-iron layered double hydroxide catalyzing oxygen evolution, *Appl. Catal. B Environ.* 314 (2022), 121491, <https://doi.org/10.1016/j.apcatb.2022.121491>.
- Y. Chen, J. Wang, Z. Yu, Y. Hou, R. Jiang, M. Wang, J. Huang, J. Chen, Y. Zhang, H. Zhu, Functional group scission-induced lattice strain in chiral macromolecular metal-organic framework arrays for electrocatalytic overall water splitting, *Appl. Catal. B Environ.* 307 (2022), 121151, <https://doi.org/10.1016/j.apcatb.2022.121151>.
- Y. Zhu, X. Liu, S. Jin, H. Chen, W. Lee, M. Liu, Y. Chen, Anionic defect engineering of transition metal oxides for oxygen reduction and evolution reactions, *J. Mater. Chem. A* 7 (2019) 5875–5897, <https://doi.org/10.1039/C8TA12477A>.
- J. Wang, J. Liu, B. Zhang, F. Cheng, Y. Ruan, X. Ji, K. Xu, C. Chen, L. Miao, J. Jiang, Stabilizing the oxygen vacancies and promoting water-oxidation kinetics in cobalt oxides by lower valence-state doping, *Nano Energy* 53 (2018) 144–151, <https://doi.org/10.1016/j.nanoen.2018.08.022>.
- K. Zhu, F. Shi, X. Zhu, W. Yang, The roles of oxygen vacancies in electrocatalytic oxygen evolution reaction, *Nano Energy* 73 (2020), 104761, <https://doi.org/10.1016/j.nanoen.2020.104761>.
- N. Yao, R. Meng, F. Wu, Z. Fan, G. Cheng, W. Luo, Oxygen-Vacancy-Induced CeO₂/Co₃N heterostructures toward enhanced pH-Universal hydrogen evolution reactions, *Appl. Catal. B Environ.* 277 (2020), 119282, <https://doi.org/10.1016/j.apcatb.2020.119282>.
- A. Demessence, A. Mesbah, M. François, G. Rogez, P. Rabu, Structure and magnetic properties of a new 1D Nickel(II) hydroxythiophenedicarboxylate, *Eur. J. Inorg. Chem.* 2009 (2009) 3713–3720, <https://doi.org/10.1002/ejic.200900329>.
- Y. Guo, K. Jia, F. Dai, Y. Liu, C. Zhang, J. Su, K. Wang, Hierarchical porous trimetallic NiCoFe-Se/CFP derived from Ni-Co-Fe Prussian blue analogues as efficient electrocatalyst for oxygen evolution reaction, *J. Colloid Interface Sci.* 642 (2023) 638–647, <https://doi.org/10.1016/j.jcis.2023.04.003>.
- X. Zhang, X. Fang, K. Zhu, W. Yuan, T. Jiang, H. Xue, J. Tian, Fe-doping induced electronic structure reconstruction in Ni-based metal-organic framework for improved energy-saving hydrogen production via urea degradation, *J. Phys. Chem. Lett.* 520 (2022), 230882, <https://doi.org/10.1016/j.jpowsour.2021.230882>.
- C.-P. Wang, Y. Feng, H. Sun, Y. Wang, J. Yin, Z. Yao, X.-H. Bu, J. Zhu, Self-optimized metal-organic framework electrocatalysts with structural stability and high current tolerance for water oxidation, *ACS Catal.* 11 (2021) 7132–7143, <https://doi.org/10.1021/acscatal.1c01447>.
- K. Metavarayuth, O. Ejegbavwo, G. McCarver, M.L. Myrick, T.M. Makris, K. D. Vogiatzis, S.D. Senanayake, O.M. Manley, A.M. Ebrahim, A.I. Frenkel, S. Hwang, T. Rajeshkumar, J.D. Jimenez, K. Chen, N.B. Shustova, D.A. Chen, Direct identification of mixed-metal centers in metal-organic frameworks: Cu₃(BTC)₂ transmetalated with Rh²⁺ ions, *J. Phys. Chem. Lett.* 11 (2020) 8138–8144, <https://doi.org/10.1021/acs.jpcclett.0c02539>.
- T. Zhao, C. Cheng, D. Wang, D. Zhong, G. Hao, G. Liu, J. Li, Q. Zhao, Preparation of a bimetallic NiFe-MOF on nickel foam as a highly efficient electrocatalyst for oxygen evolution reaction, *ChemistrySelect* 6 (2021) 1320–1327, <https://doi.org/10.1002/slct.202004504>.
- M. Salmanion, M.M. Najafpour, Structural changes of a NiFe-based metal-organic framework during the oxygen-evolution reaction under alkaline conditions, *Int. J. Hydrog. Energy* 46 (2021) 19245–19253, <https://doi.org/10.1016/j.ijhydene.2021.03.107>.
- Y. Liu, X. Hua, C. Xiao, T. Zhou, P. Huang, Z. Guo, B. Pan, Y. Xie, Heterogeneous spin states in ultrathin nanosheets induce subtle lattice distortion to trigger efficient hydrogen evolution, *J. Am. Chem. Soc.* 138 (2016) 5087–5092, <https://doi.org/10.1021/jacs.6b00858>.
- C. Feng, C. Chen, G. Xiong, D. Yang, Z. Wang, Y. Pan, Z. Fei, Y. Lu, Y. Liu, R. Zhang, X. Li, Cr-doping regulates Mn₂O₄ spinel structure for efficient total oxidation of propane: structural effects and reaction mechanism determination, *Appl. Catal. B Environ.* 328 (2023), 122528, <https://doi.org/10.1016/j.apcatb.2023.122528>.
- F. Li, Y. Tian, S. Su, C. Wang, D.-S. Li, D. Cai, S. Zhang, Theoretical and experimental exploration of tri-metallic organic frameworks (t-MOFs) for efficient electrocatalytic oxygen evolution reaction, *Appl. Catal. B Environ.* 299 (2021), 120665, <https://doi.org/10.1016/j.apcatb.2021.120665>.
- X. Mu, H. Yuan, H. Jing, F. Xia, J. Wu, X. Gu, C. Chen, J. Bao, S. Liu, S. Mu, Superior electrochemical water oxidation in vacancy defect-rich 1.5 nm ultrathin trimetal-organic framework nanosheets, *Appl. Catal. B Environ.* 296 (2021), 120095, <https://doi.org/10.1016/j.apcatb.2021.120095>.
- Y. Tang, Q. Liu, L. Dong, H.B. Wu, X.-Y. Yu, Activating the hydrogen evolution and overall water splitting performance of NiFe LDH by cation doping and plasma reduction, *Appl. Catal. B Environ.* 266 (2020), 118627, <https://doi.org/10.1016/j.apcatb.2020.118627>.
- M. Yang, M. Zhao, J. Yuan, J. Luo, J. Zhang, Z. Lu, D. Chen, X. Fu, L. Wang, C. Liu, Oxygen vacancies and interface engineering on amorphous/crystalline CrOx-Ni₃N heterostructures toward high-durability and kinetically accelerated water splitting, *Small* 18 (2022), 2106554, <https://doi.org/10.1002/smll.202106554>.
- Y. Luo, X. Yang, L. He, Y. Zheng, J. Pang, L. Wang, R. Jiang, J. Hou, X. Guo, L. Chen, Structural and electronic modulation of iron-based bimetallic

- metal–organic framework bifunctional electrocatalysts for efficient overall water splitting in alkaline and seawater environment, *ACS Appl. Mater. Interfaces* 14 (2022) 46374–46385, <https://doi.org/10.1021/acscami.2c05181>.
- [39] A. Goswami, D. Ghosh, D. Pradhan, K. Biradha, In situ grown Mn(II) MOF upon nickel foam acts as a robust self-supporting bifunctional electrode for overall water splitting: a bimetallic synergistic collaboration strategy, *ACS Appl. Mater. Interfaces* 14 (2022) 29722–29734, <https://doi.org/10.1021/acscami.2c04304>.
- [40] C.F. Li, L.J. Xie, J.W. Zhao, L.F. Gu, H.B. Tang, L. Zheng, G.R. Li, Interfacial Fe–O–Ni–O–Fe bonding regulates the active Ni sites of Ni–MOFs via iron doping and decorating with FeOOH for super-efficient oxygen evolution, *Angew. Chem. Int. Ed.* 61 (2022), e202116934, <https://doi.org/10.1002/anie.202116934>.
- [41] F. Sun, G. Wang, Y. Ding, C. Wang, B. Yuan, Y. Lin, NiFe-based metal–organic framework nanosheets directly supported on nickel foam acting as robust electrodes for electrochemical oxygen evolution reaction, *Adv. Energy Mater.* 8 (2018), 1800584, <https://doi.org/10.1002/aenm.201800584>.
- [42] Y. Li, M. Yuan, H. Yang, K. Shi, Z. Sun, H. Li, C. Nan, G. Sun, Quantitative decorating Ni-sites for water-oxidation with the synergy of electronegative sites and high-density spin state, *Appl. Catal. B Environ.* 323 (2023), 122167, <https://doi.org/10.1016/j.apcatb.2022.122167>.
- [43] J. Suntivich, K.J. May, H.A. Gasteiger, J.B. Goodenough, Y. Shao-Horn, A perovskite oxide optimized for oxygen evolution catalysis from molecular orbital principles, *Science* 334 (2011) 1383–1385, <https://doi.org/10.1126/science.1212858>.
- [44] B. Fei, Z. Chen, J. Liu, H. Xu, X. Yan, H. Qing, M. Chen, R. Wu, Ultrathinning nickel sulfide with modulated electron density for efficient water splitting, *Adv. Energy Mater.* 10 (2020), 2001963, <https://doi.org/10.1002/aenm.202001963>.
- [45] B. Tian, H. Shin, S. Liu, M. Fei, Z. Mu, C. Liu, Y. Pan, Y. Sun, W.A. Goddard 3rd, M. Ding, Double-exchange-induced in situ conductivity in nickel-based oxyhydroxides: an effective descriptor for electrocatalytic oxygen evolution, *Angew. Chem. Int. Ed.* 60 (2021) 16448–16456, <https://doi.org/10.1002/anie.202101906>.
- [46] M. Görlin, P. Cherev, J. Ferreira de Araújo, T. Reier, S. Dresch, B. Paul, R. Krähnert, H. Dau, P. Strasser, Oxygen evolution reaction dynamics, faradaic charge efficiency, and the active metal redox states of Ni–Fe oxide water splitting electrocatalysts, *J. Am. Chem. Soc.* 138 (2016) 5603–5614, <https://doi.org/10.1021/jacs.6b00332>.
- [47] Y. Zhu, H.A. Tahini, Z. Hu, Z.-G. Chen, W. Zhou, A.C. Komarek, Q. Lin, H.-J. Lin, C.-T. Chen, Y. Zhong, M.T. Fernández-Díaz, S.C. Smith, H. Wang, M. Liu, Z. Shao, Boosting oxygen evolution reaction by creating both metal ion and lattice-oxygen active sites in a complex oxide, *Adv. Mater.* 32 (2020), 1905025, <https://doi.org/10.1002/adma.201905025>.
- [48] M. Asnavandi, Y. Yin, Y. Li, C. Sun, C. Zhao, Promoting oxygen evolution reactions through introduction of oxygen vacancies to benchmark NiFe–OOH catalysts, *ACS Energy Lett.* 3 (2018) 1515–1520, <https://doi.org/10.1021/acscenergylett.8b00696>.
- [49] Z. Li, Y. Zhou, M. Xie, H. Cheng, T. Wang, J. Chen, Y. Lu, Z. Tian, Y. Lai, G. Yu, High-density cationic defects coupling with local alkaline-enriched environment for efficient and stable water oxidation, *Angew. Chem. Int. Ed.* 62 (2023), e202217815, <https://doi.org/10.1002/anie.202217815>.
- [50] W. Zhao, C. Luo, Y. Lin, G.-B. Wang, H.M. Chen, P. Kuang, J. Yu, Pt–Ru dimer electrocatalyst with electron redistribution for hydrogen evolution reaction, *ACS Catal.* 12 (2022) 5540–5548, <https://doi.org/10.1021/acscatal.2c00851>.
- [51] J. Huang, Y. Li, Y. Zhang, G. Rao, C. Wu, Y. Hu, X. Wang, R. Lu, Y. Li, J. Xiong, Identification of key reversible intermediates in self-reconstructed nickel-based hybrid electrocatalysts for oxygen evolution, *Angew. Chem. Int. Ed.* 58 (2019) 17458–17464, <https://doi.org/10.1002/anie.201910716>.
- [52] S. Ye, J. Wang, J. Hu, Z. Chen, L. Zheng, Y. Fu, Y. Lei, X. Ren, C. He, Q. Zhang, J. Liu, Electrochemical construction of low-crystalline CoOOH nanosheets with short-range ordered grains to improve oxygen evolution activity, *ACS Catal.* 11 (2021) 6104–6112, <https://doi.org/10.1021/acscatal.1c01300>.
- [53] W. Wu, Z. Gao, Q. Li, Z. Wang, S. Liu, H. Wu, Y. Zhao, Y. Jiao, X. Zhao, Structural transformation of metal–organic framework with constructed tetravalent nickel sites for efficient water oxidation, *J. Energy Chem.* 74 (2022) 404–411, <https://doi.org/10.1016/j.jechem.2022.07.040>.
- [54] B. Wang, X. Han, C. Guo, J. Jing, C. Yang, Y. Li, A. Han, D. Wang, J. Liu, Structure inheritance strategy from MOF to edge-enriched NiFe–LDH array for enhanced oxygen evolution reaction, *Appl. Catal. B Environ.* 298 (2021), 120580, <https://doi.org/10.1016/j.apcatb.2021.120580>.
- [55] M. Liu, L. Kong, X. Wang, J. He, X.-H. Bu, Engineering bimetal synergistic electrocatalysts based on metal–organic frameworks for efficient oxygen evolution, *Small* 15 (2019), 1903410, <https://doi.org/10.1002/smll.201903410>.
- [56] Z. Xiao, Y.-C. Huang, C.-L. Dong, C. Xie, Z. Liu, S. Du, W. Chen, D. Yan, L. Tao, Z. Shu, G. Zhang, H. Duan, Y. Wang, Y. Zou, R. Chen, S. Wang, Operando identification of the dynamic behavior of oxygen vacancy-rich Co₃O₄ for oxygen evolution reaction, *J. Am. Chem. Soc.* 142 (2020) 12087–12095, <https://doi.org/10.1021/jacs.0c00257>.
- [57] Y. Hu, Z. Huang, Q. Zhang, T. Taylor Isimjan, Y. Chu, Y. Mu, B. Wu, Z. Huang, X. Yang, L. Zeng, Interfacial engineering of Co_{5.47}N/Mo₅N₆ nanosheets with rich active sites synergistically accelerates water dissociation kinetics for Pt-like hydrogen evolution, *J. Colloid Interface Sci.* 643 (2023) 455–464, <https://doi.org/10.1016/j.jcis.2023.04.028>.
- [58] K. Fan, H. Zou, Y. Ding, N.V.R.A. Dharanipragada, L. Fan, A.K. Inge, L. Duan, B. Zhang, L. Sun, Sacrificial W facilitates self-reconstruction with abundant active sites for water oxidation, *Small* 18 (2022), 2107249, <https://doi.org/10.1002/smll.202107249>.
- [59] L. Li, X. Cao, J. Huo, J. Qu, W. Chen, C. Liu, Y. Zhao, H. Liu, G. Wang, High valence metals engineering strategies of Fe/Co/Ni-based catalysts for boosted OER electrocatalysis, *J. Energy Chem.* 76 (2023) 195–213, <https://doi.org/10.1016/j.jechem.2022.09.022>.
- [60] W.-D. Zhang, Q.-T. Hu, L.-L. Wang, J. Gao, H.-Y. Zhu, X. Yan, Z.-G. Gu, In-situ generated Ni–MOF/LDH heterostructures with abundant phase interfaces for enhanced oxygen evolution reaction, *Appl. Catal. B Environ.* 286 (2021), 119906, <https://doi.org/10.1016/j.apcatb.2021.119906>.
- [61] L. Yang, L. Huang, Y. Yao, L. Jiao, In-situ construction of lattice-matching NiP₂/NiSe₂ heterointerfaces with electron redistribution for boosting overall water splitting, *Appl. Catal. B Environ.* 282 (2021), 119584, <https://doi.org/10.1016/j.apcatb.2020.119584>.
- [62] S. Sun, X. Zhou, B. Cong, W. Hong, G. Chen, Tailoring the d-band centers endows (Ni_xFe_{1-x})₂P nanosheets with efficient oxygen evolution catalysis, *ACS Catal.* 10 (2020) 9086–9097, <https://doi.org/10.1021/acscatal.0c01273>.
- [63] L. Peng, J. Wang, Y. Nie, K. Xiong, Y. Wang, L. Zhang, K. Chen, W. Ding, L. Li, Z. Wei, Dual-ligand synergistic modulation: a satisfactory strategy for simultaneously improving the activity and stability of oxygen evolution electrocatalysts, *ACS Catal.* 7 (2017) 8184–8191, <https://doi.org/10.1021/acscatal.7b01971>.
- [64] Y. Zhai, X. Ren, Y. Sun, D. Li, B. Wang, S. Liu, Synergistic effect of multiple vacancies to induce lattice oxygen redox in NiFe-layered double hydroxide OER catalysts, *Appl. Catal. B Environ.* 323 (2023), 122091, <https://doi.org/10.1016/j.apcatb.2022.122091>.
- [65] Y. Li, M. Yuan, H. Yang, K. Shi, Z. Sun, H. Li, C. Nan, G. Sun, Quantitative decorating Ni-sites for water-oxidation with the synergy of electronegative sites and high-density spin state, *Appl. Catal. B Environ.* 323 (2023), 122167, <https://doi.org/10.1016/j.apcatb.2022.122167>.
- [66] C.-F. Li, J.-W. Zhao, L.-J. Xie, J.-Q. Wu, Q. Ren, Y. Wang, G.-R. Li, Surface-adsorbed carboxylate ligands on layered double hydroxides/metal–organic frameworks promote the electrocatalytic oxygen evolution reaction, *Angew. Chem. Int. Ed.* 60 (2021) 18129–18137, <https://doi.org/10.1002/anie.202104148>.
- [67] C.-F. Li, L.-J. Xie, J.-W. Zhao, L.-F. Gu, H.-B. Tang, L. Zheng, G.-R. Li, Interfacial Fe–O–Ni–O–Fe bonding regulates the active Ni sites of Ni–MOFs via iron doping and decorating with FeOOH for super-efficient oxygen evolution, *Angew. Chem. Int. Ed.* 61 (2022), e202116934, <https://doi.org/10.1002/anie.202116934>.
- [68] L. Trotochaud, S.L. Young, J.K. Ranney, S.W. Boettcher, Nickel–iron oxyhydroxide oxygen-evolution electrocatalysts: the role of intentional and incidental iron incorporation, *J. Am. Chem. Soc.* 136 (2014) 6744–6753, <https://doi.org/10.1021/ja502379c>.
- [69] M.W. Louie, A.T. Bell, An investigation of thin-film Ni–Fe oxide catalysts for the electrochemical evolution of oxygen, *J. Am. Chem. Soc.* 135 (2013) 12329–12337, <https://doi.org/10.1021/ja405351s>.